

## Article

# Catalytic CO Oxidation and H<sub>2</sub>O<sub>2</sub> Direct Synthesis over Pd and Pt-Impregnated Titania Nanotubes

Lucas Warmuth <sup>1</sup>, Gülperi Nails <sup>2</sup>, Maria Casapu <sup>2</sup>, Sheng Wang <sup>3</sup>, Silke Behrens <sup>3</sup>, Jan-Dierk Grunwaldt <sup>2,3</sup>  
and Claus Feldmann <sup>1,\*</sup>

<sup>1</sup> Institute for Inorganic Chemistry, Karlsruhe Institute of Technology (KIT), Engesserstraße 15, 76131 Karlsruhe, Germany; lucas.warmuth3@kit.edu

<sup>2</sup> Institute for Chemical Technology and Polymer Chemistry (ICTP), Karlsruhe Institute of Technology (KIT), Engesserstraße 20, 76131 Karlsruhe, Germany; guelperi.cavusoglu@kit.edu (G.N.); maria.casapu@kit.edu (M.C.); grunwaldt@kit.edu (J.-D.G.)

<sup>3</sup> Institute of Catalysis Research and Technology (IKFT), Karlsruhe Institute of Technology (KIT), Hermann-von-Helmholtz-Platz 1, 76344 Eggenstein-Leopoldshafen, Germany; sheng.wang@kit.edu (S.W.); silke.behrens@kit.edu (S.B.)

\* Correspondence: claus.feldmann@kit.edu

**Abstract:** Titania nanotubes (TNTs) impregnated with Pd and Pt nanoparticles are evaluated as heterogeneous catalysts in different conditions in two reactions: catalytic CO oxidation (gas phase, up to 500 °C) and H<sub>2</sub>O<sub>2</sub> direct synthesis (liquid phase, 30 °C). The TNTs are obtained via oxidation of titanium metal and the intermediate layer-type sodium titanate Na<sub>2</sub>Ti<sub>3</sub>O<sub>7</sub>. Thereafter, the titanate layers are exfoliated and show self-rolling to TNTs, which, finally, are impregnated with Pd or Pt nanoparticles at room temperature by using Pd(ac)<sub>2</sub> and Pt(ac)<sub>2</sub>. The resulting crystalline Pd/TNTs and Pt/TNTs are realized with different lengths (long TNTs: 2.0–2.5 μm, short TNTs: 0.23–0.27 μm) and a specific surface area up to 390 m<sup>2</sup>/g. The deposited Pd and Pt particles are 2–5 nm in diameter. The TNT-derived catalysts show good thermal (up to 500 °C) and chemical stability (in liquid-phase and gas-phase reactions). The catalytic evaluation results in a low CO oxidation light-out temperature of 150 °C for Pt/TNTs (1 wt-%) and promising H<sub>2</sub>O<sub>2</sub> generation with a productivity of 3240 mol<sub>H<sub>2</sub>O<sub>2</sub></sub> kg<sub>Pd</sub><sup>-1</sup> h<sup>-1</sup> (Pd/TNTs, 5 wt-%, 30 °C). Despite their smaller surface area, long TNTs outperform short TNTs with regard to both CO oxidation and H<sub>2</sub>O<sub>2</sub> formation.

**Keywords:** titania; nanotubes; catalysis; CO oxidation; H<sub>2</sub>O<sub>2</sub> direct synthesis



**Citation:** Warmuth, L.; Nails, G.; Casapu, M.; Wang, S.; Behrens, S.; Grunwaldt, J.-D.; Feldmann, C. Catalytic CO Oxidation and H<sub>2</sub>O<sub>2</sub> Direct Synthesis over Pd and Pt-Impregnated Titania Nanotubes. *Catalysts* **2021**, *11*, 949. <https://doi.org/10.3390/catal11080949>

Academic Editors: Ulla Simon, Maged F. Bekheet and Mino Tasbihi

Received: 23 June 2021

Accepted: 5 August 2021

Published: 8 August 2021

**Publisher's Note:** MDPI stays neutral with regard to jurisdictional claims in published maps and institutional affiliations.



**Copyright:** © 2021 by the authors. Licensee MDPI, Basel, Switzerland. This article is an open access article distributed under the terms and conditions of the Creative Commons Attribution (CC BY) license (<https://creativecommons.org/licenses/by/4.0/>).

## 1. Introduction

Specific surface area and pore volume constitute the key parameters of materials used for heterogeneous catalysis [1,2]. In this regard, several concepts and classes of materials have been discussed and studied. Predominately, this includes small-sized nanoparticles and thin films, nanomaterials with special shapes (e.g., tetrapods or spikecubes), particles with inner surfaces and pores (e.g., hollow nanospheres or nanofoams), and high-porosity bulk materials (e.g., metalorganic frameworks (MOFs) or zeolites) [3–6]. Furthermore, the interaction between the active sites and the support material has been shown to significantly affect the catalytic activity [7]. In particular, titania and ceria are known to strongly influence the structure of supported noble metal particles or highly dispersed clusters [8]. Besides the catalytic efficiency, chemical and thermal stability are naturally highly relevant, since the catalytic reactions require certain activation energy, and thus elevated temperatures [1–6].

Titania nanorods and nanotubes are of specific interest for heterogeneous catalysis, as they combine several advantages [9]. Due to their specific shape, they intrinsically offer a high surface area. The shape also promises certain thermal stability. Moreover, the ion conductivity of TiO<sub>2</sub> is significantly lower as compared to ZrO<sub>2</sub> or CeO<sub>2</sub>, which reduces

sintering effects at elevated temperatures. Until now, titania nanorods and nanotubes have been predominately used for photocatalysis, electrocatalysis, or sensing/biosensing [10–13]. Promising results were also reported for catalytic CO oxidation, most often for metal-doped  $\text{TiO}_2$  [14–16].

In the following, we evaluate the catalytic properties of titania nanotubes (TNTs) impregnated by Pd or Pt nanoparticles at different conditions, including the catalytic CO oxidation as a gas-phase reaction at temperatures up to 500 °C and the direct synthesis of  $\text{H}_2\text{O}_2$  in the liquid phase near room temperature. In addition to the different catalytic reactions, TNTs are evaluated for the first time with long and short lengths. CO oxidation over Pt/TNTs resulted in low light-off/light-out temperatures.  $\text{H}_2\text{O}_2$  direct synthesis over Pd/TNTs, to the best of our knowledge, is also reported for the first time.

## 2. Results and Discussion

### 2.1. Synthesis, Exfoliation and Nanotube Formation

The preparation of Pd/TNT and Pt/TNT catalysts was performed by liquid-phase synthesis of the TNTs and impregnation with the noble metal thereafter (Figure 1). First of all, titanium metal powder was oxidized in aqueous sodium hydroxide to obtain the layer-type sodium titanate  $\text{Na}_2\text{Ti}_3\text{O}_7$ . Here, it should be noted that the oxidation was not performed by electrochemical oxidation but by a simple liquid-phase process only. The crystalline structure of  $\text{Na}_2\text{Ti}_3\text{O}_7$  exhibits  $\infty^2[\text{Ti}_3\text{O}_{14/2}]^{2-}$  layers parallel to the crystallographic  $b,c$  plane with edge- and corner-sharing ( $\text{TiO}_6$ ) octahedra [17], which are separated by  $\text{Na}^+$  cations (Figure 1). By acidic treatment, the  $\text{Na}^+$  cations can be exchanged by  $\text{H}^+$ , which resulted in an exfoliation of the titanate layers [18]. Due to the high charge and the lacking lattice energy, the titanate layers are unstable in the liquid phase and instantaneously show self-rolling to the more stable TNTs (Figure 1). This liquid-phase strategy also allows us to prepare longer and shorter TNTs. With this in mind, the titanium metal powder was oxidized in NaOH for 24 h at 120 °C, followed by exfoliation and self-rolling in  $\text{HNO}_3$  to obtain long TNTs. The formation of short TNTs was performed similarly; however, the alkaline oxidation in NaOH was accelerated by the addition of concentrated  $\text{H}_2\text{O}_2$ . This results in a faster oxidation, and thus, short TNTs.

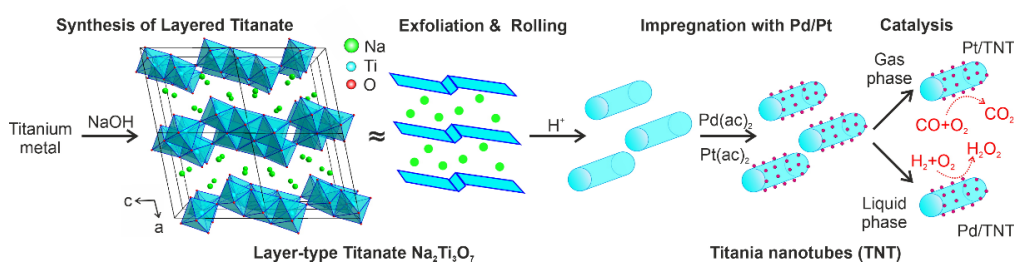


**Figure 1.** Scheme of the synthesis strategy starting from the oxidation of titanium metal via the formation and exfoliation of the layer-type titanate  $\text{Na}_2\text{Ti}_3\text{O}_7$  to TNTs as well as the impregnation with Pd and Pt to obtain Pd/TNTs and Pt/TNTs.

Subsequent to oxidation, exfoliation and self-rolling process, the as-prepared TNTs were washed by centrifugation/redispersion in/from water to remove all remains of starting materials and salts. Finally, the TNTs were impregnated with Pd or Pt (Figure 1). After that, a solution of  $\text{Pd}(\text{ac})_2$  or  $\text{Pt}(\text{ac})_2$  in acetone was dropped on the TNT powder. This procedure offers two advantages. On the one hand,  $\text{Pd}(\text{ac})_2$  or  $\text{Pt}(\text{ac})_2$  can be reduced by reducing gas ( $\text{N}_2:\text{H}_2 = 10:90$ ) already at room temperature. On the other hand, the low surface tension of acetone results in an instantaneous distribution of the  $\text{Pd}(\text{ac})_2$  or  $\text{Pt}(\text{ac})_2$  solution via capillary forces. This promotes both a homogenous distribution as well as the formation of small metal particles, and is therefore preferred over the more common use of solutions of palladium or platinum chlorides or nitrates in water. Taken together, this liquid-phase strategy is also suitable to reliably obtain sufficient quantities of Pd/TNTs and Pt/TNTs.

## 2.2. Nanotube Structure with Pd or Pt Impregnation

The size and shape of the as-prepared TNTs were examined by transmission electron microscopy (TEM, Figure 2). The TEM overview and detailed images clearly point to the difference between the long TNTs with a length of  $2200 \pm 300$  nm (Figure 2a) and the short TNTs with a length of  $250 \pm 50$  nm (Figure 2b). Detailed images portray the nanotube structure with the lighter, less-electron-absorbing center of the nanotube. The diameter of the long TNTs is about 20–30 nm, whereas the diameter of the short TNTs is about 10–20 nm. The difference between long and short TNTs was also confirmed by nitrogen sorption analysis and the resulting specific surface area and pore volume, which were deduced via the Brunauer–Emmett–Teller (BET) and the Barrett–Joyner–Halenda (BJH) formalism (Figure 2c). Accordingly, the long TNTs exhibit a specific surface area of  $214 \text{ m}^2/\text{g}$  and a pore volume of  $0.237 \text{ cm}^3/\text{g}$  (Table 1). The short TNTs show even higher values of  $390 \text{ m}^2/\text{g}$  and  $0.695 \text{ cm}^3/\text{g}$ . To the best of our knowledge, this specific surface area belongs to the highest values reported for  $\text{TiO}_2$  in the literature. Thus,  $\text{TiO}_2$  with a specific surface area  $< 300 \text{ m}^2/\text{g}$  was observed most often [19–23]. Values of about  $300 \text{ m}^2/\text{g}$  were, however, only reported for nanorods and microspheres [24,25], as well as for  $\text{TiO}_2$ - $\text{SiO}_2$  composite xerogels [26,27].

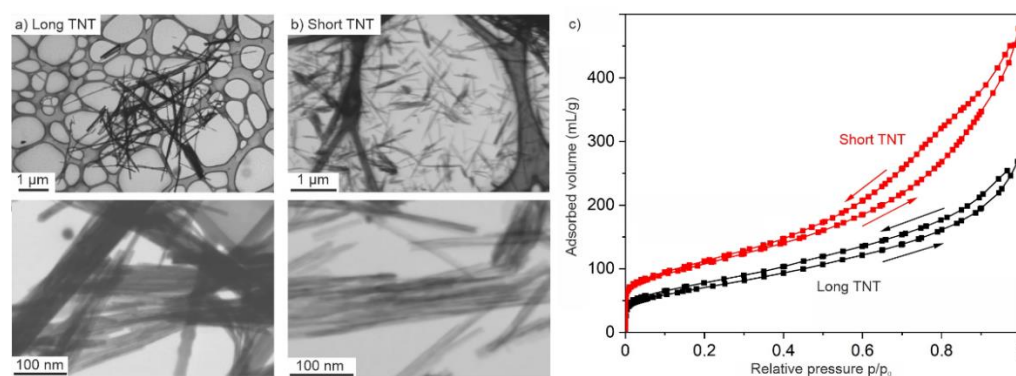


**Figure 2.** Long and short TNTs: (a) TEM overview and detail images of long TNTs, (b) TEM overview and detail images of short TNTs, (c) nitrogen sorption analysis of long and short TNTs.

**Table 1.** Specific surface area and pore volume of TNTs prior to and after impregnation with Pd or Pt.

Material	Specific Surface Area ( $\text{m}^2/\text{g}$ )	Pore Volume ( $\text{cm}^3/\text{g}$ )
TNTs (long) <sup>1</sup>	214	0.237
Pt/TNTs (long) <sup>1</sup>	201	0.640
Pd/TNTs (long) <sup>1</sup>	193	0.467
TNTs (short) <sup>2</sup>	387	0.695
Pt/TNTs (short) <sup>2</sup>	379	0.941
Pd/TNTs (short) <sup>2</sup>	369	0.830

<sup>1</sup> Long TNTs were obtained by slow oxidation of titanium metal in NaOH. <sup>2</sup> Short TNTs were obtained by fast oxidation of titanium metal in NaOH/ $\text{H}_2\text{O}_2$ .

In addition to size, shape and surface area, the crystallinity and thermal stability of the TNTs were examined. According to X-ray powder diffraction analysis (XRD), the as-prepared TNTs are already crystalline, as indicated by weak but clearly visible Bragg reflections (Figure 3a). Here, the Bragg peaks at 24 and 48 degree of two-theta are in coincidence with the two most intense peaks of anatase. An additional Bragg peak at 9 degree of two-theta is significantly broader and, according to the literature, points to exfoliated titanate layers and are associated with the TNT surface [28,29]. Subsequent to certain sintering at  $400 \text{ }^\circ\text{C}$  in air, the TNTs are well-crystallized and show all characteristic Bragg peaks of anatase (Figure 3a). Exposure to  $400 \text{ }^\circ\text{C}$  did also not affect the TNT structure. According to high-resolution (HR)TEM images, the nanotube structure is maintained after

the thermal treatment process (Figure 3b). Highly parallel lattice fringes in the nanotube wall indicate the crystallinity of the TNTs (Figure 3b,c). Fast Fourier transformations (FFT) of selected areas on HRTEM images also confirm the crystallinity. Here, all observed Bragg peaks are in agreement with the tetragonal anatase modification of  $\text{TiO}_2$  (Figure 3d). In sum, the TNTs show good thermal stability, as was already observed for such nanotubes [29–31]. Decomposition of the TNT structure was observed to start at temperatures  $> 500\text{ }^\circ\text{C}$  and is triggered by the phase transformation from anatase to rutile.

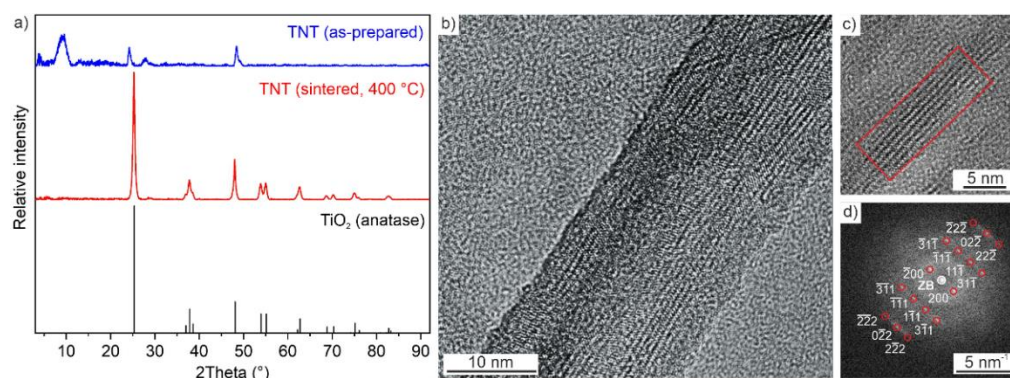


**Figure 3.** Crystallinity of the TNTs: (a) X-ray powder diffraction of the as-prepared TNTs, TNTs sintered at  $400\text{ }^\circ\text{C}$  ( $\text{TiO}_2$ /anatase as a reference: ICDD-No. 086-1157), (b) HRTEM of sintered TNTs ( $400\text{ }^\circ\text{C}$ ), (c + d) HRTEM of sintered TNTs ( $400\text{ }^\circ\text{C}$ ) with FFT analysis in (d) of the crystalline area marked with red frame in (c) (ZB: zero beam).

Finally, the size and distribution of the metal particles as well as the shape and structure of the resulting Pt/TNTs and Pd/TNTs were examined by high-angle annular dark-field scanning transmission electron microscopy (HAADF-STEM) and energy-dispersive X-ray spectroscopy (EDXS). Accordingly, the 1 wt-% Pt/TNT catalyst exhibits a homogeneous distribution with small-sized Pt nanoparticles (Figure 4). The size range of Pt nanoparticles is comparable on the long and short TNT supports, with an average metal particle size of  $4.3 \pm 1.2$  (range: 0.5–10 nm) and  $2.1 \pm 0.5$  nm (range 0.5–3 nm), respectively. This corresponds to a dispersion of 25 and 40% [1]. This rather small size can be ascribed to the mild reducing conditions applied during sample preparation ( $\text{H}_2/\text{N}_2$ , room temperature) and the high surface area of the nanorods. The specific surface area of the Pt/TNT catalysts and the as-prepared TNTs are almost similar within the measurement error. In contrast to the specific surface area, the pore volume was significantly increased for Pt/TNTs, resulting in  $0.640\text{ cm}^3/\text{g}$  for long Pt/TNTs and  $0.941\text{ cm}^3/\text{g}$  for short Pt/TNTs (Table 1). This notable increase in comparison to the as-prepared TNTs (long TNT:  $0.237\text{ cm}^3/\text{g}$ , short TNT:  $0.695\text{ cm}^3/\text{g}$ ) can be ascribed to pores formed due to metal nanoparticle deposition as well as due to pores between the TNTs that only become available if the Pd or Pt nanoparticles are present on the TNT surface as spacers.

The 5 wt-% Pd/TNTs show similar features as the Pt/TNTs. Thus, size, shape and surface area are very comparable to the as-prepared TNTs (Figure 5). Again, a homogeneous distribution of Pd nanoparticles with an average size of  $3.8 \pm 1.0$  nm (long Pd/TNTs) and  $3.7 \pm 1.4$  nm (short Pd/TNTs) was observed all over the long and short TNT supports using HAADF-STEM images and EDXS element maps. In contrast to the specific surface area, the pore volume is again significantly increased for Pd/TNTs (long Pd/TNT:  $0.467\text{ cm}^3/\text{g}$ , short Pd/TNT:  $0.830\text{ cm}^3/\text{g}$ ) in comparison to the as-prepared TNTs (long TNT:  $0.237\text{ cm}^3/\text{g}$ , short Pd/TNT:  $0.695\text{ cm}^3/\text{g}$ , Table 1). Similar to Pt/TNTs, this finding can be attributed to the formation of additional pores between the Pd-impregnated TNTs.

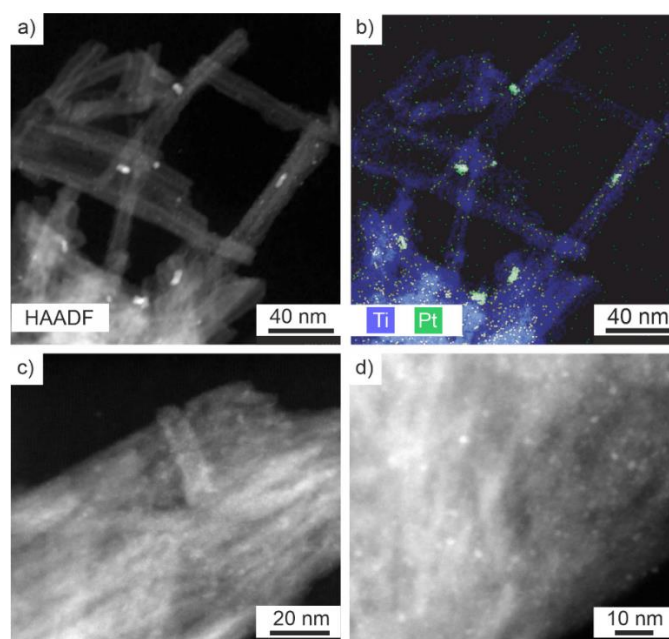


**Figure 4.** TEM analysis of Pt/TNTs: (a) HAADF-STEM image of long Pt/TNTs with (b) EDXS element map. (c) HAADF-STEM image of short Pt/TNTs with (d) HRTEM image.

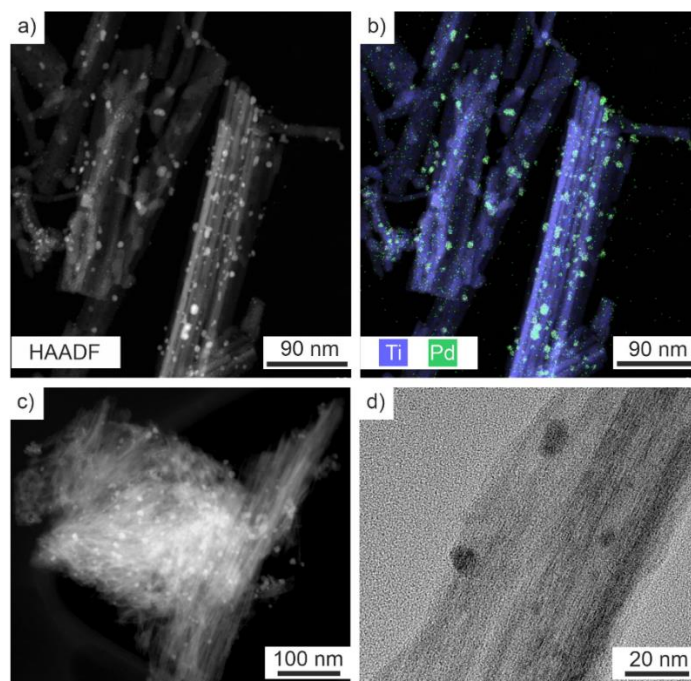


**Figure 5.** TEM analysis of Pd/TNTs: (a) HAADF-STEM image of long Pd/TNTs with (b) EDXS element map. (c) HAADF-STEM image of short Pd/TNTs with (d) HRTEM image.

### 2.3. Catalytic CO Oxidation and H<sub>2</sub>O<sub>2</sub> Direct Synthesis

The catalytic properties of the as-prepared Pd/TNT and Pt/TNT samples were evaluated at different conditions with two exemplary reactions. This includes CO oxidation (Figure 6), which was performed as a solid/gas-phase reaction at temperatures up to 500 °C, and H<sub>2</sub>O<sub>2</sub> direct synthesis (Figure 7), which was conducted in the liquid phase at 30 °C. Both reactions are technically relevant for emission control [32] and decentralized production of H<sub>2</sub>O<sub>2</sub> from H<sub>2</sub> and O<sub>2</sub> [33,34].

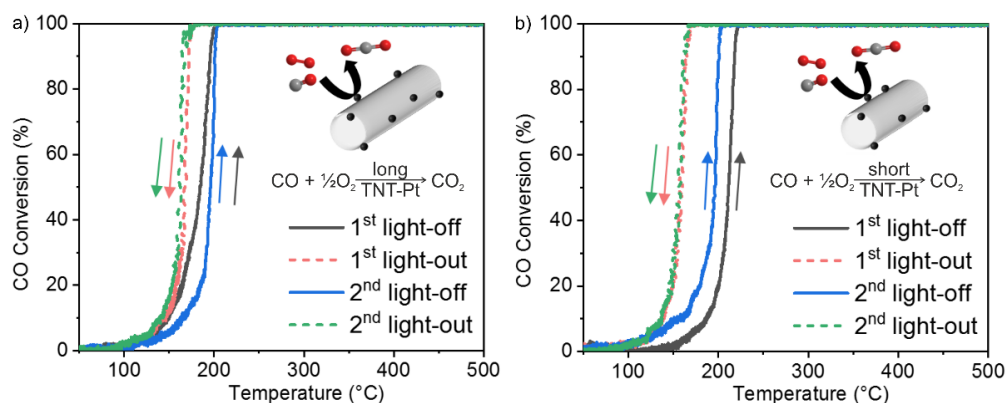


**Figure 6.** Catalytic CO oxidation with Pt/TNTs (1 wt-%) with (a) long Pt/TNTs and (b) short Pt/TNTs.

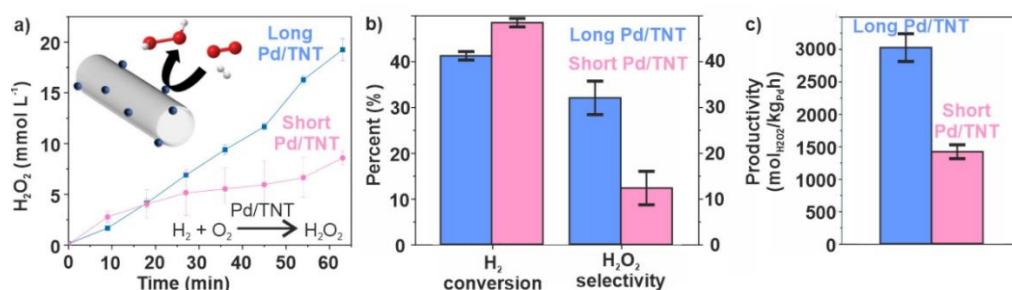


**Figure 7.** H<sub>2</sub>O<sub>2</sub> direct synthesis with Pd/TNT (5 wt-%) with (a) concentration over time, (b) H<sub>2</sub> conversion and H<sub>2</sub>O<sub>2</sub> selectivity, and (c) H<sub>2</sub>O<sub>2</sub> productivity for long and short Pd/TNTs.

CO oxidation was tested with the 1 wt-% Pt/TNT samples. The catalyst was deposited in quartz microreactors ( $\varnothing$ : 1.5 mm) and exposed to a gas mixture of 1000 ppm of CO and 10% of O<sub>2</sub> in He at ambient pressure between 50–500 °C. The outlet gas composition was analyzed by Fourier-transform infrared (FT-IR) spectroscopy and mass spectrometry (MS). The long Pt/TNT catalyst shows slightly better CO oxidation activity during the first light-off/light-out cycle compared to the catalyst supported on short TNTs (Figure 6: black/red arrows). The light-off and light-out temperatures (50% of activity reached) were 185 and 165 °C for the long Pt/TNT catalyst (Figure 6a), whereas the same CO conversion was measured at 210 and 157 °C, respectively, for the short Pt/TNT catalyst (Figure 6b). A higher temperature for CO oxidation light-off generally corresponds to the prevalent presence of very small (<2 nm) or larger (>5 nm) Pt particles [35]. According to TEM images (Figure 4), the first situation seems to be present for the short Pt/TNT catalyst, whereas the slightly larger noble metal particles deposited on the long-TNTs sustain the low-temperature CO oxidation better. This hypothesis is also supported by the approximately 25 °C shift in the light-off curve towards lower temperature observed for the short Pt/TNT sample during the second CO oxidation cycle. At the same time, a 10 °C higher temperature was measured for the long Pt/TNT catalyst, which contains larger Pt nanoparticles. Such changes can be ascribed to certain settling of the catalyst, such as the crystallization of TiO<sub>2</sub> or a change in the electronic state of the noble metal.

BET surface area measurements conducted after a mild thermal treatment up to 400 °C indicate a decrease from 201 to 166 m<sup>2</sup>/g (long Pt/TNTs) and 379 m<sup>2</sup>/g to 321 m<sup>2</sup>/g (short Pt/TNTs). Although about a 15% loss of specific surface was observed in both cases, the dispersion of Pt particles should not be significantly affected by this variation, as the noble metal concentration on the titania surface is far below a monolayer concentration [36]. Instead, it is the dynamics of the Pt nanoparticles at the respective temperature which is strongly influenced by the initial particle size and interaction with the TiO<sub>2</sub> support. For

TiO<sub>2</sub>, the mobility of the noble metal on surface has been controversially discussed with respect to differently exposed TiO<sub>2</sub> facets [37]. For a weak interaction with the support [38], certain sintering of the small Pt particles on the short Pt/TNT catalyst (average size  $2.1 \pm 0.5$  nm) could occur during heating up to 500 °C in the reaction mixture. Such a change would correlate with the observed improvement in activity during the second CO oxidation cycle and with the narrower hysteresis with the light-out temperature at 155 °C (Figure 6: blue/green arrows). According to previous studies, slightly larger Pt particles (2–3 nm) are beneficial for CO oxidation due to their higher resistance to oxidation, as metallic Pt was found to be the active species for this reaction [39]. The light-out temperature of the second cycle for long Pt/TNTs is very similar to that measured during the first light-out, suggesting that a certain thermal and chemical steadiness has been reached already after the first catalytic cycle. Here, a mild sintering process involving very small noble metal nanoparticles might occur also on the long TNT support. Due to the already existing larger Pt particles on long Pt/TNTs (average size  $4.3 \pm 1.2$  nm vs.  $2.1 \pm 0.5$  nm for the short Pt/TNTs), however, the overall effect can be expected to be lower as compared to the short Pt/TNTs. For both long and short Pt/TNTs, moreover, certain influence due to a thermal removal of precursor traces might occur during the first heating step, but can be expected to be similar for both samples.

In order to demonstrate our hypothesis on the sintering of smaller Pt nanoparticles, five temperature cycles were conducted between room temperature and 500 °C for the as-prepared Pt/TNT catalysts. Electron microscopy did not indicate any noticeable change in the Pt particle size for the long Pt/TNT sample. Thus, the size of the Pt nanoparticles remained constant within the significance of the experiment ( $4.3 \pm 1.2$  nm prior to heating cycles;  $4.1 \pm 1.0$  nm after five heating cycles). In contrast, the size of the Pt nanoparticles supported on the short TNT support increased from  $2.1 \pm 0.5$  to  $5.2 \pm 1.1$  nm after five heating cycles. Accordingly, the initially higher surface area and the smaller size of the Pt nanoparticles of the short Pt/TNTs do not seem to be beneficial for achieving a higher CO oxidation performance relative to the long Pt/TNT catalyst.

In the second part of our study, H<sub>2</sub>O<sub>2</sub> direct synthesis was performed over the Pd/TNT (5 wt-%) catalyst suspended in ethanol at 30 °C and 40 bar. Prior to the reaction, the catalyst suspension was treated with reducing gas (H<sub>2</sub>:N<sub>2</sub> = 4:96). Thereafter, the suspension was vigorously stirred, and the reaction gas mixture (H<sub>2</sub>:O<sub>2</sub>:N<sub>2</sub> = 4:20:76) was introduced into the reactor. H<sub>2</sub>, O<sub>2</sub> and N<sub>2</sub> leaving the reactor were periodically analyzed using a micro-GC. The H<sub>2</sub>O<sub>2</sub> concentration was analyzed ex situ by UV-Vis spectroscopy (Figure 7a) [40]. As a result, the as-prepared Pd/TNT catalysts show a H<sub>2</sub> conversion of 42% and 49% as well as a H<sub>2</sub>O<sub>2</sub> selectivity of 32% and 13% in the case of long Pd/TNTs and short Pd/TNTs, respectively (Figure 7b). Moreover, a productivity of  $3240 \text{ mol}_{\text{H}_2\text{O}_2} \cdot \text{kg}_{\text{Pd}}^{-1} \cdot \text{h}^{-1}$  was observed for the long Pd/TNT catalyst and  $1452 \text{ mol}_{\text{H}_2\text{O}_2} \cdot \text{kg}_{\text{Pd}}^{-1} \cdot \text{h}^{-1}$  in the case of short Pd/TNTs (Figure 7c).

Similar to the aforementioned CO oxidation, the long Pd/TNTs again outperform the short Pd/TNTs in terms of H<sub>2</sub>O<sub>2</sub> selectivity and productivity. Under these reaction conditions, the long Pd/TNTs show a high H<sub>2</sub>O<sub>2</sub> productivity with respect to a Pd nanoparticle-derived reference catalyst on acid-pretreated, commercial TiO<sub>2</sub> (P25) [40]. Compared to Pd catalysts supported on conventional TiO<sub>2</sub>, the long Pd/TNTs revealed an especially high H<sub>2</sub>O<sub>2</sub> productivity, particularly in the case of a non-electrochemical catalytic process of direct H<sub>2</sub>O<sub>2</sub> synthesis [32,33]. This could be related to the higher stability of the Pd nanoparticles and the lower curving of the surface of long Pd/TNTs. It should be also emphasized that these catalytic tests were carried out in absence of additional acid or halide promoters. Thus, it is to be expected that the activity, H<sub>2</sub>O<sub>2</sub> productivity and especially the H<sub>2</sub>O<sub>2</sub> selectivity can be further increased under optimized reaction conditions in the presence of these promoters. However, in terms of industrial application, the addition of large amounts of inorganic acids to the solvent would require corrosion-resistant and thus expensive reactor materials [33]. In addition, leaching of active metal is accelerated at low pH, leading to catalyst deactivation. In general, the role of support materials in direct H<sub>2</sub>O<sub>2</sub>

synthesis has been studied in quite some detail, and their properties (e.g., acidity, polarity, and metal support interactions) may influence the reaction. In a few cases, TNTs have been examined with regard to  $\text{H}_2\text{O}_2$  direct synthesis, but without any specific data on selectivity and conversion rate [32,33].

### 3. Materials and Methods

#### 3.1. Synthesis

*General.* Titanium (98.7%, ABCR, Karlsruhe, Germany), NaOH ( $\geq 97.0\%$ , VWR),  $\text{H}_2\text{O}_2$  (medical pure, 30%, Sigma Aldrich, Taufkirchen, Germany),  $\text{Pd}(\text{ac})_2$  (47.5% Pd, Acros Organics, Fair Lawn, USA), acetone (technical grade, Seulberger, Karlsruhe, Germany), and  $\text{HNO}_3$  (technical grade, 65%, AppliChem, Darmstadt, Germany) were used as purchased.

*Synthesis of  $\text{Pt}(\text{ac})_2$ .*  $\text{Pt}(\text{ac})_2$  was prepared according to the literature [36]. Thus, 1.02 g  $\text{PtCl}_2$  (99.99%, Sigma Aldrich, Taufkirchen Germany), and 1.35 g  $\text{Ag}(\text{ac})$  ( $>98.0\%$ , Sigma Aldrich) were dissolved in 60 mL acetic acid (99%, VWR, Karlsruhe, Germany) and refluxed for 45 min. The precipitated solid (i.e.,  $\text{AgCl}$ ) was centrifuged and the blue solution thereafter dried with reduced pressure.  $\text{Pt}(\text{ac})_2$  was then dissolved in dichloromethane (99.5%, VWR), filtered over a glass frit, and the obtained solution again dried with reduced pressure. Finally, the resulting blue  $\text{Pt}(\text{ac})_2$  was dissolved in diethylether (99.5%, Carl Roth, Karlsruhe, Germany), filtered again, and dried with reduced pressure.

*Synthesis of titania nanotubes (TNTs).* The synthesis was conducted according to a procedure reported by Kasuga et al. [18]. Accordingly, 120 mg of Ti powder was dispersed in 40 mL of 10 M NaOH and heated in a Teflon-lined autoclave to 120 °C for 24 h. After natural cooling, the colorless solid was washed three times by centrifugation/redispersion in/from deionized water and resuspended in 50 mL of 0.175 M  $\text{HNO}_3$ . This suspension was treated on an orbital shaker for 12 h. The protonation was repeated once. After washing, the resulting long TNTs were washed three times by centrifugation/redispersion in/from deionized water. Finally, the TNTs were dried at 70 °C. In the case of short TNTs, the solvent was a mixture of 30 mL of 10 M NaOH and 10 mL of 30%  $\text{H}_2\text{O}_2$ .

*$\text{Pd}/\text{TNTs}$  (5 wt-%).*  $\text{Pd}(\text{ac})_2$  was dissolved in 15 mL of acetone. The resulting yellow solution was then added to the aforementioned TNTs by drop-casting to obtain a yellow to orange powder, which was dried under vacuum and directly purged with  $\text{H}_2/\text{N}_2$  (10:90). The color of the  $\text{Pd}/\text{TNT}$  powder turned to black, indicating the formation of elemental Pd.

*$\text{Pt}/\text{TNTs}$  (1 wt-%).*  $\text{Pt}(\text{ac})_2$  was dissolved in 15 mL of acetone. The resulting yellow solution was then added to the aforementioned TNTs by drop-casting to obtain a yellow powder, which was then dried under vacuum and directly purged with  $\text{H}_2/\text{N}_2$  (10:90) at room temperature. The color change of the  $\text{Pt}/\text{TNT}$  powder to deep black indicates the formation of elemental Pt.

#### 3.2. Analytical Equipment

*Field emission scanning electron microscopy (FESEM,* Zeiss Supra 40VP, Oberkochen, Germany) was used to determine the morphology of the as-prepared TNTs and their variations in the scanning transmission electron microscopy (STEM) mode. Samples were prepared by casting one drop of an aqueous suspension on a 300 mesh copper grid with Lacey carbon film.

*Transmission electron microscopy (TEM) and energy dispersive X-ray spectroscopy (EDXS)* were conducted with a FEI Osiris microscope operated at 200 kV (FEI, Eindhoven, The Netherlands). The FEI Osiris microscope was equipped with a Bruker Quantax system (XFlash detector, Bruker, Ettlingen, Germany). EDX spectra were quantified with the FEI software package “TEM imaging and analysis” (TIA). TEM samples were prepared by putting a drop of suspension of the respective powder sample in ethanol onto a copper grid coated with an amorphous carbon (Lacey)-supporting film. Average particle diameters were calculated by statistical evaluation of at least 150 nanoparticles (ImageJ 1.47v software).

*X-ray powder diffraction.* Crystallinity and chemical composition of the TNT,  $\text{Pd}/\text{TNT}$ , and  $\text{Pt}/\text{TNT}$  samples were examined with a Stoe STADI-MP diffractometer (Stoe, Darm-

stadt, Germany), equipped with Ge-monochromator and Cu- $K_{\alpha 1}$  radiation. About 10 mg of the respective sample was deposited on an acetate foil and fixed with scotch tape.

*Volumetric sorption measurements* was carried out with an AUTOSORB IQ-XR VITON (Anton Paar, Graz, Austria), applying  $N_2$  as the adsorbate. Specific surface area was determined using Brunauer–Emmett–Teller (BET) theory, and pore analysis was performed using density functional theory (DFT), respectively. Prior to the analysis, the TNT samples were dried at 120 °C in vacuum.

### 3.3. Catalysis

*CO oxidation.* For the catalytic activity tests, Pt/TNTs (1 wt-%) were used in the form of a sieved granulate fraction (125–250  $\mu\text{m}$ ). CO oxidation was performed in quartz microreactors (inner diameter: 1.5 mm) with atmospheric pressure at 50–500 °C (heating rate: 5 °C/min). The gas mixture (1000 ppm CO, 10%  $O_2$  in He) was applied with a total gas flow of 50 mL/min (GHSV: 60.000  $\text{h}^{-1}$ ). Thereafter, the gas composition was detected continuously on-line by an FTIR spectrometer (Multigas 2000, MKS Instruments, Munich, Germany) and by mass spectrometry (Omnistar, Pfeiffer Vacuum, Asslar, Deutschland) at the reactor outlet (CO consumption,  $CO_2$  formation).

*$H_2O_2$  direct synthesis* was performed in a semi-continuous 300 mL batch reactor (30 °C, 40 bar). The semi-continuous batch reactor was operated as a batch reactor with respect to the liquid phase containing the suspended catalyst, whereas the gas phase ( $H_2/O_2/N_2$  4/20/76) was continuously supplied during the reaction (total flow of 250  $\text{mL}_{\text{NTP}}/\text{min}$ ) [40]. The Pd/TNTs (1.3 mg Pd per experiment) were suspended in ethanol as the reaction medium (200 mL). Before starting the reaction, the catalyst suspension was activated with  $H_2$  (4 vol-% in  $N_2$ , 250  $\text{mL}_{\text{NTP}}/\text{min}$ , 30 °C, 40 bar) for 1 h. Thereafter, the educt–gas mixture was introduced and stirring was started (1000 rpm). It should be noted that the flammable and explosive nature of  $H_2/O_2$  is a point of great concern: 4 vol%  $H_2$  represents the lower flammability limit for  $H_2$  in air and thus, for safety reasons, the  $H_2$  concentration should never exceed 4 vol% under these conditions.  $H_2$ ,  $O_2$  and  $N_2$  concentrations leaving the reactor were periodically determined by micro-GC (GC: gaschromatography).  $N_2$  was used as an internal standard. The  $H_2O_2$  concentration was analyzed ex situ by UV-Vis spectroscopy.  $H_2$  conversion and  $H_2O_2$  selectivity were determined after 63 min of the reaction. Each test was repeated. The catalysts were handled in air.

## 4. Conclusions

In summary, titania nanotubes (TNTs) were prepared in a liquid-phase process, starting with the controlled oxidation of titanium metal and the formation of  $Na_2Ti_3O_7$  as a layer-type titanate. Thereafter, the titanate layers were exfoliated and instantaneously show self-rolling to TNTs. Depending on the speed of oxidation (i.e., alkaline conditions only or alkaline conditions with  $H_2O_2$ ), long TNTs (i.e., slow oxidation) and short TNTs (fast oxidation) can be obtained. Finally, Pd or Pt nanoparticles were deposited on the TNTs using incipient wetness impregnation and mild reduction. Thus, using solutions of  $Pd(ac)_2$  or  $Pt(ac)_2$  in acetone leads to a homogeneous distribution and a uniform coverage of the TNTs with small Pd or Pt nanoparticles due to capillary forces and a reduction in the metals at room temperature. Crystalline Pd/TNT and Pt/TNT catalysts were obtained with lengths of 2.0–2.5  $\mu\text{m}$  (long TNTs) or 0.23–0.27  $\mu\text{m}$  (short TNTs) and specific surface areas up to 214 (long TNTs) and 390  $\text{m}^2/\text{g}$  (short TNTs). The Pd and Pt particles were 2–5 nm in diameter.

The catalytic properties of the long and short Pd/TNTs and Pt/TNTs were evaluated with two different experimental conditions using two catalytic test reactions. This includes the catalytic CO oxidation as a solid phase-gas phase reaction at temperatures up to 500 °C and the  $H_2O_2$  direct synthesis from hydrogen and oxygen in the liquid phase at 30 °C. Promising catalytic activity was observed for CO oxidation with light-out temperatures of 150 °C for long Pt/TNTs (1 wt-%), as well as with regard to a  $H_2O_2$  selectivity and productivity of 32% and 3240  $\text{mol}_{H_2O_2} \cdot \text{kg}_{Pd}^{-1} \cdot \text{h}^{-1}$  for long Pd/TNTs (5 wt-%). Despite

the significantly smaller surface area, the catalysts supported on long TNTs interestingly outperform those on short TNTs with regard to both CO oxidation and H<sub>2</sub>O<sub>2</sub> formation, which can be related to more pronounced sintering and mobility of the metal nanoparticles on the more curved surface of short TNTs. Moreover, the TNTs show good chemical and shape stability as a catalyst support up to temperatures of 500 °C. Based on the feasibility of the synthesis and the promising catalytic activity at different experimental conditions, Pd/TNTs and Pt/TNTs can be interesting catalyst systems. Further improvement, for instance, with regard to the optimal concentration and particle size of the noble metals, catalyst (pre-)treatment or the addition of specific promoters will be necessary to further improve the catalytic performance.

**Author Contributions:** L.W. performed the synthesis and characterization of the materials, which was supervised by C.F., G.N. performed the CO oxidation, with supervision and discussion in the broad context by M.C. and J.-D.G., S.W. performed the catalytic H<sub>2</sub>O<sub>2</sub> synthesis, which was supervised by S.B., L.W. and C.F. wrote the manuscript, which was corrected by all authors. All authors have read and agreed to the published version of the manuscript.

**Funding:** The authors acknowledge the Deutsche Forschungsgemeinschaft (DFG) for funding within the Collaborative Research Centers “Tracking the Active Site in Heterogeneous Catalysis for Emission Control” (CRC1441). Moreover, L.W. acknowledges the Studienstiftung des deutschen Volkes for a scholarship.

**Data Availability Statement:** The datasets generated during and/or analyzed during the current study are available from the corresponding author on reasonable request.

**Acknowledgments:** The authors acknowledge the Laboratory for electron microscopy (LEM) at the KIT and specifically D. Gerthsen and R. Popescu for excellent TEM support. We also acknowledge J. Eckel and Y. Träutlein for support with respect to catalytic testing in direct H<sub>2</sub>O<sub>2</sub> synthesis.

**Conflicts of Interest:** The authors declare no conflict of interest.

## References

1. Ertl, G.; Knözinger, H.; Weitkamp, J. (Eds.) *Handbook of Heterogeneous Catalysis*; VCH: Weinheim, Germany, 1997; Volume 2.
2. Trovarelli, A.; Llorca, J. Ceria catalysts at nanoscale: How do crystal shapes shape catalysis? *ACS Catal.* **2017**, *7*, 4716–4735. [[CrossRef](#)]
3. Janssen, A.; Nguyen, Q.; Xia, Y. Colloidal metal nanocrystals with metastable crystal structures. *Angew. Chem. Int. Ed.* **2021**, *60*, 12192–12203. [[CrossRef](#)] [[PubMed](#)]
4. Gilroy, K.D.; Yang, X.; Xie, S.; Zhao, M.; Qin, D.; Xia, Y. Shape-controlled synthesis of colloidal metal nanocrystals by replicating the surface atomic structure on the seed. *Adv. Mater.* **2018**, *30*, 1706312. [[CrossRef](#)] [[PubMed](#)]
5. Kubacka, A.; Fernandez-Garcia, M.; Colon, G. Advanced nanoarchitectures for solar photocatalytic applications. *Chem. Rev.* **2012**, *112*, 1555–1614. [[CrossRef](#)] [[PubMed](#)]
6. Stock, N.; Biswas, S. Synthesis of metal-organic frameworks (MOFs): Routes to various MOF topologies, morphologies, and composites. *Chem. Rev.* **2012**, *112*, 933–969. [[CrossRef](#)] [[PubMed](#)]
7. Van Deelen, T.W.; Hernández Mejía, C.; de Jong, K.P. Control of metal-support interactions in heterogeneous catalysts to enhance activity and selectivity. *Nat. Catal.* **2019**, *2*, 955–970. [[CrossRef](#)]
8. Zhang, S.; Plessow, P.N.; Willis, J.J.; Dai, S.; Xu, M.; Graham, G.W.; Cargnello, M.; Abild-Pedersen, F.; Pan, X. Dynamical observation and detailed description of catalysts under strong metal-support interaction. *Nano Lett.* **2016**, *16*, 4528–4534. [[CrossRef](#)]
9. Musselwhite, N.; Somorjai, G.A. Investigations of structure sensitivity in heterogeneous catalysis: From single crystals to monodisperse nanoparticles. *Top. Catal.* **2013**, *56*, 1277–1283. [[CrossRef](#)]
10. Schneider, J.; Matsuoka, M.; Takeuchi, M.; Zhang, J.; Horiuchi, Y.; Anpo, M.; Bahnemann, D.W. Understanding TiO<sub>2</sub> photocatalysis: Mechanisms and materials. *Chem. Rev.* **2014**, *114*, 919–9986. [[CrossRef](#)] [[PubMed](#)]
11. Xue, S.-G.; Tang, L.; Tang, Y.-K.; Li, C.-X.; Li, M.-L.; Zhou, J.-J.; Chen, W.; Zhu, F.; Jiang, J. Selective electrocatalytic water oxidation to produce H<sub>2</sub>O<sub>2</sub> using a C,N codoped TiO<sub>2</sub> electrode in an acidic electrolyte. *ACS Appl. Mater. Interfaces* **2020**, *12*, 4423–4431. [[CrossRef](#)] [[PubMed](#)]
12. Zheng, J.; Huang, K.; Hou, G.; Zhang, H.; Cao, H. A highly active Pt nanocatalysts supported on RuO<sub>2</sub> modified TiO<sub>2</sub>-NTs for methanol electrooxidation with excellent CO tolerance. *Int. J. Hydrog. Energy* **2019**, *44*, 31506–31514. [[CrossRef](#)]
13. Cheng, Z.; Gu, Z.; Chen, J.; Yu, J.; Zhou, L. Synthesis, characterization, and photocatalytic activity of porous La-N-co-doped TiO<sub>2</sub> nanotubes for gaseous chlorobenzene oxidation. *J. Environ. Sci.* **2016**, *46*, 203–213. [[CrossRef](#)] [[PubMed](#)]
14. Camposeco, R.; Hinojosa-Reyes, M.; Castillo, S.; Nava, N.; Zanella, R. Synthesis and characterization of highly dispersed bimetallic Au-Rh nanoparticles supported on titanate nanotubes for CO oxidation reaction at low temperature. *Environ. Sci. Pollut. Res.* **2021**, *28*, 10734–10748. [[CrossRef](#)] [[PubMed](#)]

15. Guo, J.; Han, Q.; Zhong, S.; Zhu, B.; Huang, W.; Zhang, S. Au/M-TiO<sub>2</sub> nanotube catalysts (M = Ce, Ga, Co, Y): Preparation, characterization and their catalytic activity for CO oxidation. *J. Sol-Gel Sci. Technol.* **2018**, *86*, 699–710. [[CrossRef](#)]
16. Krick, C.; Grabau, M.; Yoo, J.E.; Killian, M.; Schmuki, P.; Steinrueck, H.P.; Papp, C. Reactivity of TiO<sub>2</sub> nanotube-supported Pt particles in the CO oxidation reaction. *ChemCatChem* **2017**, *9*, 564–572. [[CrossRef](#)]
17. Andersson, S.; Wadsley, A.D. The crystal structure of Na<sub>2</sub>Ti<sub>3</sub>O<sub>7</sub>. *Acta Crystallogr.* **1961**, *14*, 1245–1249. [[CrossRef](#)]
18. Kasuga, T.; Hiramatsu, M.; Hoson, A.; Sekino, T.; Niihara, K. Titania nanotubes prepared by chemical processing. *Adv. Mater.* **1999**, *11*, 1307–1311. [[CrossRef](#)]
19. Ling, Y.; Zhang, M.; Li, X.; Zheng, J.; Xu, J. Formation of uniform mesoporous TiO<sub>2</sub>@C-Ni hollow hybrid composites. *Dalton Trans.* **2018**, *47*, 10093–10101. [[CrossRef](#)] [[PubMed](#)]
20. Wang, X.; Bai, L.; Liu, H.; Yu, X.; Yin, Y.; Gao, C.A. Unique disintegration-reassembly route to mesoporous titania nanocrystalline hollow spheres with enhanced photocatalytic activity. *Adv. Funct. Mater.* **2018**, *28*, 1704208. [[CrossRef](#)]
21. Wang, W.; Xu, D.; Cheng, B.; Yu, J.; Jiang, C. Hybrid carbon@TiO<sub>2</sub> hollow spheres with enhanced photocatalytic CO<sub>2</sub> reduction activity. *J. Mater. Chem. A* **2017**, *5*, 5020–5029. [[CrossRef](#)]
22. Liu, H.; Li, W.; Shen, D.; Zhao, D.; Wang, G. Graphitic carbon conformal coating of mesoporous TiO<sub>2</sub> hollow spheres for high-performance lithium ion battery anodes. *J. Am. Chem. Soc.* **2015**, *137*, 13161–13166. [[CrossRef](#)]
23. Bu, D. Biotemplated synthesis of high specific surface area copper-doped hollow spherical titania and its photocatalytic research for degrading chlorotetracycline. *Appl. Surf. Sci.* **2013**, *265*, 677–685. [[CrossRef](#)]
24. Weng, S.; Zhao, X.; Liu, G.; Guan, Y.; Wu, F.; Luo, Y. Synthesis, characterization, antibacterial activity in dark and in vitro cytocompatibility of Ag-incorporated TiO<sub>2</sub> microspheres with high specific surface area. *J. Mater. Sci.* **2018**, *29*, 50. [[CrossRef](#)] [[PubMed](#)]
25. Gerasimova, T.V.; Evdokimova, O.L.; Kraev, A.S.; Ivanov, V.K.; Agafonov, A.V. Micro-mesoporous anatase TiO<sub>2</sub> nanorods with high specific surface area possessing enhanced adsorption ability and photocatalytic activity. *Microporous Mesoporous Mater.* **2016**, *235*, 185–194. [[CrossRef](#)]
26. Mitrofanov, A.; Brandes, S.; Herbst, F.; Rigolet, S.; Bessmertnykh-Lemeune, A.; Beletskaya, I. Immobilization of copper complexes with (1,10-phenanthroline)phosphonates on titania supports for sustainable catalysis. *J. Mater. Chem. A* **2017**, *5*, 12216–12235. [[CrossRef](#)]
27. Zhu, W.; Yang, H.; Xie, Y.; Sun, S.; Guo, X. Hierarchically porous titania xerogel monoliths: Synthesis, characterization and electrochemical properties. *Mater. Res. Bull.* **2016**, *73*, 48–55. [[CrossRef](#)]
28. Tsai, C.-C.; Teng, H. Regulation of the physical characteristics of titania nanotube aggregates synthesized from hydrothermal treatment. *Chem. Mater.* **2004**, *16*, 4352–4358. [[CrossRef](#)]
29. Luxa, J.; Vosecký, P.; Mazánek, V.; Sedmidubský, D.; Pumera, M.; Sofer, Z. Cation-controlled electrocatalytic activity of transition-metal disulfides. *ACS Catal.* **2018**, *8*, 2774–2781. [[CrossRef](#)]
30. Acevedo-Peña, P.; Carrera-Crespo, J.E.; González, F.; González, I. Effect of heat treatment on the crystal phase composition, semiconducting properties and photoelectrocatalytic color removal efficiency of TiO<sub>2</sub> nanotubes arrays. *Electrochim. Acta* **2014**, *140*, 564–571. [[CrossRef](#)]
31. Grigorieva, A.V.; Goodilin, E.A.; Derlyukova, L.E.; Anufrieva, T.A.; Tarasov, A.B.; Dobrovolskii, Y.A.; Tretyakov, Y.D. Titania nanotubes supported platinum catalyst in CO oxidation process. *Appl. Catal. A* **2009**, *362*, 20–25. [[CrossRef](#)]
32. Deutschmann, O.; Grunwaldt, J.-D. Exhaust gas aftertreatment in mobile systems: Status, challenges, and perspectives. *Chem. Ing. Tech.* **2013**, *85*, 595–617. [[CrossRef](#)]
33. Ranganathan, S.; Sieber, V. Recent advances in the direct synthesis of hydrogen peroxide using chemical Catalysis—A review. *Catalysts* **2018**, *8*, 379. [[CrossRef](#)]
34. Dittmeyer, R.; Grunwaldt, J.-D.; Pashkova, A. A review of catalyst performance and novel reaction engineering concepts in direct synthesis of hydrogen peroxide. *Catal. Today* **2015**, *248*, 149–159. [[CrossRef](#)]
35. Casapu, M.; Fischer, A.; Gänzler, A.M.; Popescu, R.; Crone, M.; Gerthsen, D.; Türk, M.; Grunwaldt, J.D. Origin of the normal and inverse hysteresis behavior during CO oxidation over Pt/Al<sub>2</sub>O<sub>3</sub>. *ACS Catal.* **2017**, *7*, 343–355. [[CrossRef](#)]
36. Maurer, F.; Jelic, J.; Wang, J.; Gänzler, A.; Dolcet, P.; Wöll, C.; Wang, Y.; Studt, F.; Casapu, M.; Grunwaldt, J.D. Tracking the formation, fate and consequence for catalytic activity of Pt single sites on CeO<sub>2</sub>. *Nat. Catal.* **2020**, *3*, 824–833. [[CrossRef](#)]
37. Wan, Q.; Hu, S.; Dai, J.; Chen, C.; Li, W.X. Influence of crystal facet and phase of titanium dioxide on ostwald ripening of supported Pt nanoparticles from first-principles kinetics. *J. Phys. Chem. C* **2019**, *123*, 11020–11031. [[CrossRef](#)]
38. Zhou, Y.; Doronkin, D.E.; Chen, M.; Wei, S.; Grunwaldt, J.D. Interplay of Pt and crystal facets of TiO<sub>2</sub>: CO oxidation activity and operando XAS/DRIFTS studies. *ACS Catal.* **2016**, *6*, 7799–7809. [[CrossRef](#)]
39. Gänzler, A.M.; Casapu, M.; Boubnov, A.; Müller, O.; Conrad, S.; Lichtenberg, H.; Grunwaldt, J.D. Operando spatially and time-resolved X-ray absorption spectroscopy and infrared thermography during oscillatory CO oxidation. *J. Catal.* **2015**, *328*, 216–224. [[CrossRef](#)]
40. Naina, V.R.; Wang, S.; Sharapa, D.I.; Zimmermann, M.; Hähslar, M.; Niebl-Eibenstein, L.; Wang, J.; Wöll, C.; Wang, Y.; Singh, S.K.; et al. Shape-selective synthesis of intermetallic Pd<sub>3</sub>Pb nanocrystals and enhanced catalytic properties in the direct synthesis of hydrogen peroxide. *ACS Catal.* **2021**, *11*, 2288–2301. [[CrossRef](#)]